

Review article

Tectonic Assessment of the Northwestern Nubian Shield at Southern Sinai, Egypt

 Sherif Mansour^{1*}, Mohamed A. Gharib¹
¹ Geology Department, Faculty of Science, Port Said University, Egypt

Email: sherif@sci.psu.edu.eg, mohamed.sadek11@sci.psu.edu.eg

RECEIVED 8 March 2025
REVISED 16 March 2025
ACCEPTED 9 April 2025
ONLINE 11 April 2025

CITATION

Mansour, S. & Gharib, M.A., (2025).
 Tectonic Assessment of the Northwestern
 Nubian Shield at Southern Sinai, Egypt.
 Spectrum Science Journal, 2(1): 17-31
DOI: 10.21608/sasj.2025.366650.1002

CORRESPONDENCE

Sherif Mansour
 Email: sherif@sci.psu.edu.eg

The Scientific Association for Studies and
 Applied Research (SASAR)
<https://sasj.journals.ekb.eg>


COPYRIGHT

©2025 by the authors. Submitted for
 possible open access publication under the
 terms and conditions of the Creative
 Commons Attribution (CC BY) license.

Spectrum Science Journal

PRINT ISSN: 3062-5068

ONLINE ISSN: 3062-5076

Abstract:

The Gulf of Suez is a relatively young continental rift, with its boundaries composed of the Arabian–Nubian Shield basement complex, which formed during the East African Orogeny. The precise effects and significance of the repeated tectonic activities on the Arabian–Nubian Shield and their role in the rifting processes in the Gulf of Suez are still not fully understood. However, the combination of zircon and apatite fission-track dating, alongside time–temperature modeling, has proven helpful in investigating these processes. This study reviews thermochronological data derived from basement samples from the Wadis Ba’ba and Nesyrin regions, representing the northern end of the Gulf of Suez’s eastern flank. The zircon fission-track data revealed two distinct age groups for each region, approximately 652 ± 25 Ma and 426 ± 31 Ma for W. Ba’ba, and 530 ± 15 Ma and 331 ± 10 Ma for W. Nesyrin. Meanwhile, the apatite fission-track data identified three spatially distinct age groups at W. Ba’ba, dating to about 473 ± 10 Ma, 269 ± 29 Ma, and 101 ± 12 Ma, and two spatially distinct age groups at W. Nesyrin, dating to about 263 ± 13 Ma and 76 ± 7 Ma. These data represent cooling ages decreasing southward. The reconstructed time–temperature profiles indicated four significant episodes of rapid cooling, corresponding to the Neoproterozoic, Devonian–Carboniferous, Cretaceous, and Oligocene–Miocene periods. These cooling pulses were developed in response to four key tectonic events: (1) the post-accretion erosion event during the Precambrian–Cambrian, (2) the Devonian–Carboniferous Variscan tectonic event, (3) the Cretaceous break-up of Gondwana, and (4) the Oligocene–Miocene rifting of the Gulf of Suez.

Keywords: Sinai tectonic history, rift flanks, the Nubian shield, Sinai thermochronology.

I. Introduction

The Arabian-Nubian Shield (ANS) represents the largest Neoproterozoic juvenile continental crust belt on Earth (Patchett & Chase, 2002; Stern et al., 2004), formed during the East African Orogeny (Meert, 2003). The Sinai sub-plate, where the northernmost section of the ANS basement is exposed, lies within a tectonically active zone bordered by the African, Eurasian, and Arabian continental plates (Fig. 1). The ANS outcrops serve as geological archives, preserving records of tectonic events that have shaped the region since its formation in the Neoproterozoic. These tectonic processes have played a crucial role in uplifting, erosion, sedimentation, basin formation, and the evolution of landforms over time.

While the region’s tectonic history is well-established, questions remain regarding the full extent and impact of specific events, such as the post-accretion erosional event, the Variscan tectonism, the opening of the mid-Atlantic, the formation of the Syrian Arc system, the development of the Mediterranean basin, and the rifting of the Gulf of Suez in the northern part of the ANS (Hashad, 1980; Kolodner et al., 2006; Mansour, 2015, 2023a; Mansour et al., 2021; Meneisy, 1986; Schott & Schmeling, 1998; Stampfli et al., 2002).

It is well known that the post-accretion erosional event led to the uplifting and erosion of the ANS basement, though the scale of this event is still uncertain (Kolodner et al., 2006; Mansour et al., 2025; Said, 1990). To better understand the response of the ANS to tectonic events—particularly localized uplift through fault-bounded blocks from the post-accretion event to the Suez rifting—more detailed research and comparison between the different regions of studies are required (Kohn et al., 1992; Kröner et al., 1990; Mansour et al., 2023b; Mansour et al., 2024a; Omar et al., 1987; Omar & Steckler, 1995).

This study compares the fission-track data and modeling results of Mansour et al. (Mansour et al., 2024a; Mansour et al., 2025) to provide new insights into the region’s tectonic history.

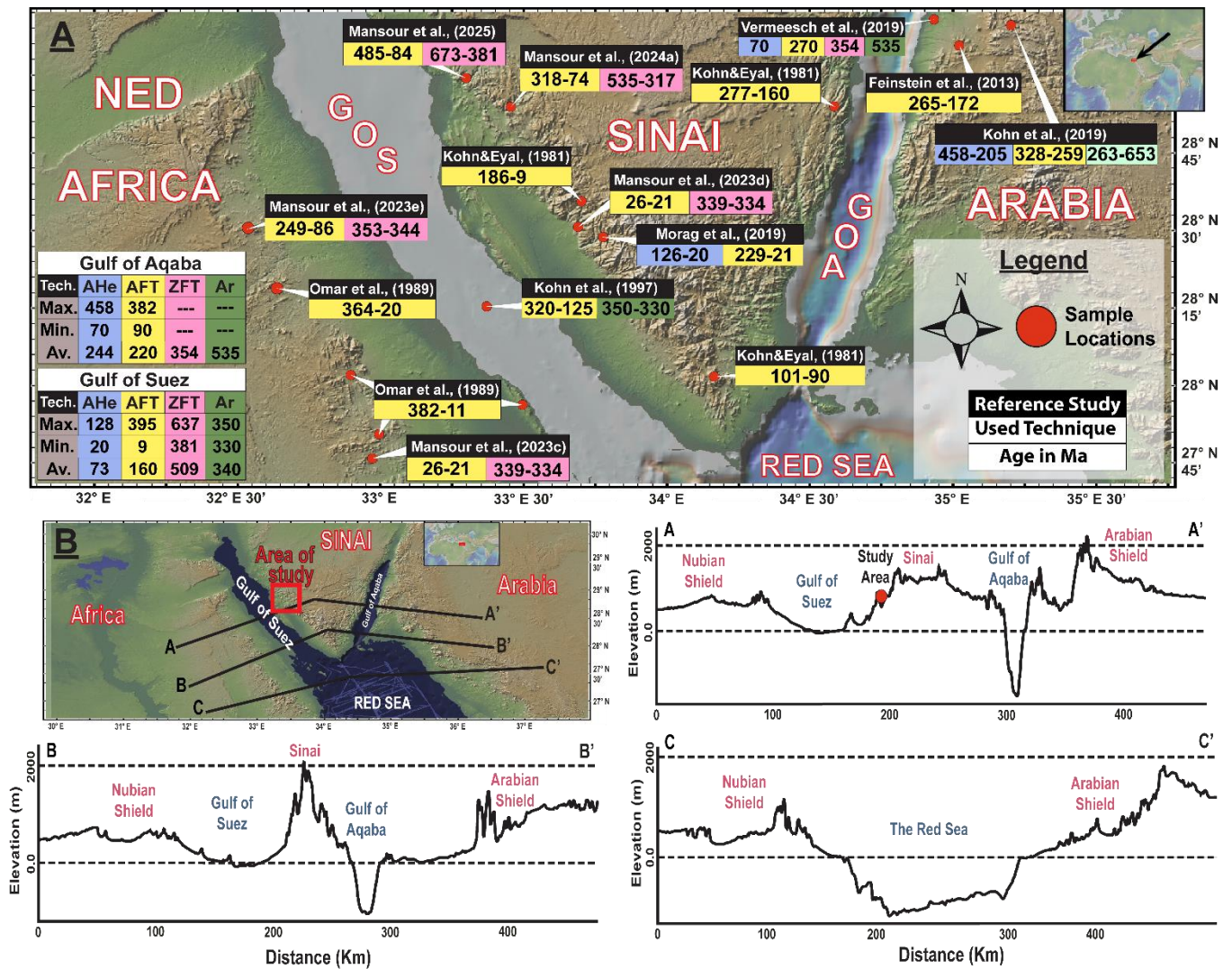
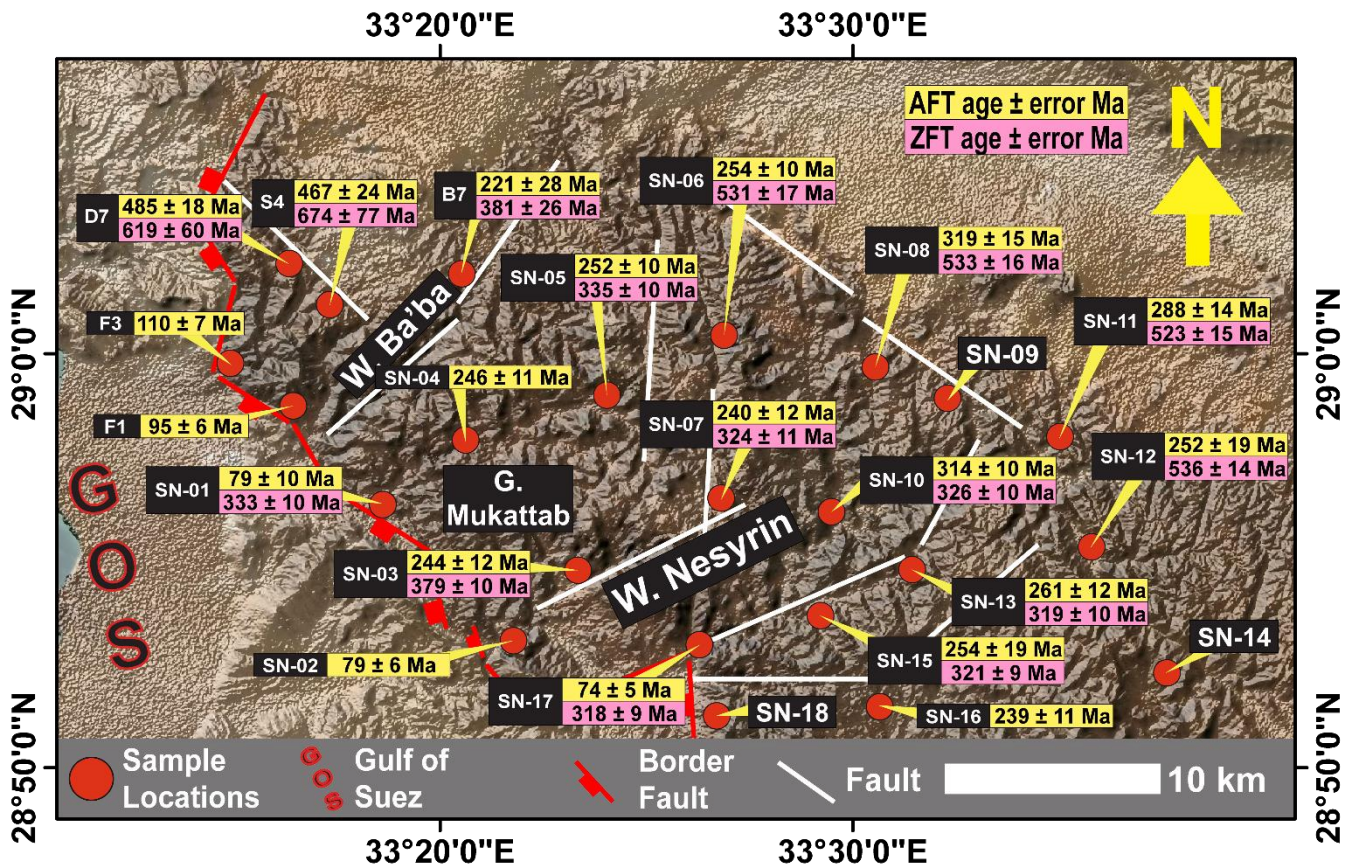


Figure 1. A. Location map based on digital elevation model with the previous thermochronological studies in Sinai and northern the ANS (modified after Mansour et al., 2022a). Where, AHe= apatite (U-Th)/He, AFT= apatite fission-track, ZHe= zircon (U-Th)/He, ZFT= zircon fission-track, and Ar= Ar-Ar dating. B. Digital elevation model expressing the Egyptian basement exposures, the area of study, Sinai triple junction, and location of topographic cross sections across the ANS. The (AA') across northern the North Eastern Desert, the Gulf of Suez (GOS), northern south Sinai, the Gulf of Aqaba (GOA), and northern Arabia, (BB') across southern the North Eastern Desert, the Gulf of Suez, southern South Sinai, the Gulf of Aqaba, and northern Arabia, (CC') across the central Eastern Desert, the Red Sea, and central Arabia.

II. Geological setting

The term Pan-African was introduced by Kennedy (1964) refers to the extensive thermo-tectonic events that shaped Gondwana around 500 million years ago. The East African Orogeny, part of the broader Pan-African Orogeny, led to the formation of the Arabian-Nubian Shield (ANS) through a series of accretion events involving oceanic plateaus, continental fragments, and island arcs that merged with Archean continental nuclei between approximately 900 and 650 million years ago (Meert, 2003). The southern Sinai, where the northern edge of the ANS basement is exposed, consists predominantly of granitoid rocks, with lesser amounts of metasedimentary, metavolcanic, and volcanic units (Fig. 1; Fig. 2).



Seilacher, 1990). This was followed by a tectonic stability period marked by platform-related sedimentation (Alsharhan & Nairn, 1997; Mansour et al., 2024a). The Variscan tectonic event, occurring during the Devonian-Carboniferous in response to the collision between Gondwana and Laurasia, resulted in substantial uplifts and erosion by the Late Carboniferous (Bojar et al., 2002; Gvirtzman & Weissbrod, 1984; Klitzsch, 1986). Consequently, much of the Lower Paleozoic sedimentary sequence was eroded in Sinai, except for small remnants found at Wadi Samra. In contrast, a 2 to 2.5 km thick Lower Paleozoic sequence has been preserved in southern Jordan and northern Saudi Arabia (Kohn et al., 1992). The East Mediterranean basin became active during the Triassic-Jurassic (Garfunkel & Derin, 1985), and Gondwana began to rift during the Jurassic-Cretaceous, influencing the Egyptian ANS through limited volcanic activity (Hashad, 1980; Klitzsch, 1986; Mansour et al., 2022a; Meneisy, 1986). Mid-Atlantic spreading during the Middle Jurassic caused the eastward movement of the African plate, ultimately suturing it with the Eurasian plate (Dewey et al., 1973). This resulted in significant magmatism in northern Egypt and the formation of normal NW-SE and N-S trending faults (Girdler, 1985; Greiling et al., 1988), as well as the development of the northeast-oriented folds of the Syrian Arc system (Awad, 1984; Moustafa et al., 2003; Said, 1962; Sakran et al., 2019; Sestini, 1984; Shehata et al., 2020). The Oligocene-Miocene rifting of the northern Red Sea and the Suez Rift system led to uplifts, erosion along the ANS margins, basaltic dikes, and the formation of normal faults. During the Middle Miocene, the Gulf of Aqaba rift became the primary boundary between the African and Arabian plates, spreading rates significantly faster (four to eight times higher) than those observed in the Suez Rift (Steckler et al., 1998).

III. Techniques and operating conditions

Fission-track (FT) thermochronometry is based on accumulating and preserving radiation-induced damage to mineral crystal lattices. This damage occurs when heavy fragments, generated by the spontaneous fission of uranium-238 (^{238}U) atoms, pass through the mineral, leaving tracks that can be revealed through chemical etching (Wagner, 1972). These fission tracks undergo annealing at distinct temperatures, which vary between different minerals (Gleadow & Duddy, 1981; Yamada et al., 1995). The thermal sensitivity of these tracks allows for the reconstruction of potential temporal and thermal (t-T) histories associated with the movement of rocks through the upper crust. The analytical approach and techniques are provided in detail by Mansour et al. (2024a).

IV. Thermochronological Results

For Mansour et al. (2025), The ZFT ages and their corresponding standard errors ranged from approximately 674 ± 77 Ma to 381 ± 26 Ma. These ages were categorized into two distinct groups based on their spatial distribution. The first group, located in the northern portion of the study area (group A), had the oldest ZFT ages, ranging from 674 ± 77 Ma to 619 ± 60 Ma. These ages spanned over about 55 million years, but they overlapped within their analytical uncertainties (Table 1), resulting in an average ZFT age of approximately 652 ± 25 Ma. The second group, consisting of the remaining samples (groups B and C), had ZFT ages ranging from approximately 462 ± 32 Ma to 381 ± 26 Ma (Table 1). These ages span a broader range of about 80 million years but overlapped within their analytical errors, yielding an average ZFT age of approximately 431 ± 31 Ma.

The AFT ages in this study ranged from 485 ± 19 Ma to 84 ± 11 Ma, which were divided into three distinct spatiotemporal groups (Table 2). Group A consisted of three samples with Cambrian-Ordovician ages, ranging from 485 ± 19 Ma to 467 ± 15 Ma (Fig. 2), providing an average AFT age of approximately 473 ± 19 Ma. Group B contained six samples with Carboniferous-Triassic AFT ages, ranging from 303 ± 13 Ma to 221 ± 28 Ma, yielding an average AFT age of approximately 269 ± 14 Ma. Group C included

five samples with Cretaceous AFT ages ranging from 110 ± 7 Ma to 84 ± 11 Ma, with an average AFT age of approximately 101 ± 7 Ma (Table 2).

Table 1 Zircon fission-track ages, data, and sample descriptions.

S.-No.	Elevation [m a.s.l.]	Coordinates Decimal		Lithology	²³⁸ U	n	ρ_s	N _s	X ²	Cen. Age	1 σ
		N	E		[μ g/g]		($\times 10^5$ track/cm ²)		[%]		
Mansour et al. (2024a)											
Group A											
SN-06	873	28.98910°	33.44455°	Syenite	276.5	15	82.5	3807	0.92	531.1	16.6
SN-08	654	28.97891°	33.54666°	Diorite	417.3	14	125.3	5080	0.96	533.1	16.2
SN-11	606	28.94663°	33.52853°	Diorite	319.2	17	93.4	4997	0.94	522.5	14.8
SN-12	834	28.93110°	33.56591°	Syenite	427.5	21	128.4	6985	0.95	535.5	13.5
Group B											
SN-01	371	28.91624°	33.33642°	Diorite	347.3	18	63.7	3911	1.00	333.2	10.0
SN-03	545	28.91351°	33.38155°	Migmatite	361.4	19	75.9	5685	1.00	378.8	10.3
SN-05	698	28.96906°	33.36418°	Syenite	283.5	18	52.6	4015	1.00	335.3	9.7
SN-07	819	28.94219°	33.45251°	Syenite	248.5	15	44.2	2038	0.99	323.5	11.3
SN-10	658	28.95223°	33.55076°	Gneiss	345.2	17	62.1	3325	1.00	325.9	9.8
SN-13	661	28.90790°	33.51673°	Gneiss	216.4	18	38.2	2201	0.99	319.4	10.4
SN-15	496	28.90193°	33.47526°	Syenite	352.8	20	62.4	3635	1.00	320.5	9.0
SN-17	344	28.87269°	33.40992°	Syenogranite	225.9	23	39.6	3327	1.00	317.9	9.1
Mansour et al. (2025)											
Group A											
D7	520	28.98060	33.29531	Diorite	136.0	17	376	2229	0.98	619.1	59.7
S4	316	29.00518	33.29181	Gneiss	177.0	13	629	1581	0.96	673.9	76.9
S10	202	29.00858	33.28718	Syenite	95.4	21	318	2981	0.95	668.3	58.1
Group B											
B7	229	28.98646	33.31475	Syenite	205.5	23	358	3546	0.99	381.4	26.1
B11	100	29.00158	33.24493	Syenite	179.7	12	390	1823	0.96	442.2	39.8
N3	299	28.94910	33.33041	Syenite	180.0	21	316	1808	0.97	419.1	37.9
Z3	192	28.94379	33.30038	Gneiss	168.9	24	384	4112	0.97	461.7	32.0
D4	298	28.96731	33.27985	Syenite	163.8	22	393	3875	0.98	452.4	31.8

The analysed samples belong to the ANS basement rocks with formation ages of are between 720 and 580 Ma (Mansour et al., 2022a). Group A (older ZFT cooling ages), B (younger ZFT ages). S.-No.; samples number, [m a.s.l.]; elevation in meters above sea-level, U; Uranium concentration in μ g/g, n; the number of counted zircon grains, ρ_s ; density of spontaneous tracks (10^5 tr/cm²), N_s; the number of spontaneous tracks. X²: the Chi-square test, Cen. Age: central ages with an uncertainty of 1-sigma calculated using IsoplotR (Vermeesch, 2018).

The results from the t-T models indicated that the samples were affected by an initial rapid cooling event during the Neoproterozoic, which brought them to or near the Earth's surface (Figs. 4-5). Following this event, three distinct groups emerged in the thermal histories of the samples:

1. Group A was affected by a Neoproterozoic cooling event, followed by slow reheating until the Late Oligocene when the samples were cooled to surface temperatures (Figs. 4-5).

2. Group B experienced Neoproterozoic cooling, followed by reheating until the Carboniferous (Figs. 4-5). This was followed by another rapid cooling event during the Devonian-Carboniferous, which increased the samples' temperatures to those of the partial annealing zone of the AFT. A phase of thermal constancy followed until the Oligocene-Miocene when the samples were cooled to surface temperatures (Figs. 4-5).

3. Group C underwent a Neoproterozoic cooling event, followed by reheating that may have lasted from the Devonian-Carboniferous to the Cretaceous (Figs. 4-5). A second fast-cooling event then affected these samples during the Jurassic-Cretaceous, cooling them to temperatures in the AFT partial annealing zone. The samples then entered a phase of thermal stability until the Oligocene-Miocene, when they were again cooled to surface temperatures (Figs. 4-5).

Table 2 Apatite fission-track ages, data and sample descriptions.

S.-No.	Elevation [m a.s.l.]	Coordinates Decimal		Lithology	²³⁸ U [µg/g]	n	ρ _s (X10 ⁶ track/cm ²)	N _s	X ² [%]	Age [Ma]	1σ	Lc no.	Lc (µm)	1σ	Dpar (µm)	1σ
		N	E													
Mansour et al. (2024a)																
Group A																
SN-01	371	28.91624°	33.33642°	Diorite	8.9	21	0.3	65	0.99	79.1	10.3	54	13.4	1.5	1.4	0.1
SN-02	480	28.89321°	33.36375°	Syenite	22.3	20	0.7	182	1.00	78.7	6.2	6	11.9	1.3	1.5	0.1
SN-17	344	28.87269°	33.40992°	Syenogranite	21.9	20	0.8	250	1.00	73.7	5.4	80	12.4	1.6	1.5	0.1
SN-18	432	28.83123°	33.43687°	Diorite	NA	NA	NA	NA	NA	NA	NA	NA	NA	NA	NA	NA
Group B																
SN-03	545	28.91351°	33.38155°	Migmatite	32.5	17	3.7	638	0.99	244.1	11.9	70	12.5	1.2	1.5	0.1
SN-04	517	28.96758°	33.41586°	Syenite	27.2	22	3.1	667	0.99	246.0	11.1	7	12.1	0.9	1.5	0.1
SN-05	698	28.96906°	33.36418°	Syenite	35.2	20	5.2	1120	1.00	251.6	9.9	85	13.2	1.1	1.5	0.1
SN-06	873	28.98910°	33.44455°	Syenite	22.0	20	2.7	681	1.00	254.2	10.4	100	13.2	1.2	1.4	0.1
SN-07	819	28.94219°	33.45251°	Syenite	27.8	20	3.2	519	0.97	239.8	11.9	109	13.1	1.2	1.5	0.1
SN-08	721	28.99807°	33.52186°	Syenite	10.4	20	2.2	464	0.93	318.9	15.3	94	13.3	1.1	1.5	0.1
SN-09	717	28.98177°	33.54415°	Diorite	NA	NA	NA	NA	NA	NA	NA	NA	NA	NA	NA	NA
SN-10	658	28.95223°	33.55076°	Gneiss	16.2	20	3.0	1013	1.00	314.3	10.2	108	13.2	1.2	1.4	0.1
SN-11	606	28.94663°	33.52853°	Diorite	23.8	20	3.6	569	0.94	288.2	14.3	8	11.8	1.2	1.5	0.1
SN-12	834	28.93110°	33.56591°	Syenite	40.0	20	6.1	1452	0.92	251.9	19.2	81	13.2	1.0	1.5	0.1
SN-13	661	28.90790°	33.51673°	Gneiss	18.2	20	2.7	698	0.97	261.1	12.4	12	12.3	1.4	1.4	0.1
SN-14	863	28.90091°	33.58210°	Syenite	NA	NA	NA	NA	NA	NA	NA	NA	NA	NA	NA	NA
SN-15	496	28.90193°	33.47526°	Syenite	41.2	22	6.0	1343	0.92	253.7	19.3	103	13.2	1.3	1.5	0.1
SN-16	664	28.88317°	33.49553°	Diorite	21.8	20	3.0	575	0.98	239.2	11.2	5	12.6	1.0	1.4	0.1
Mansour et al. (2025)																
Group A																
D7	525	28.992403	33.257961	Syenite	7.5	18	2.5	1198	86	484.5	18.2	53	12.4	1.0	1.6	0.2
D8	520	28.994728	33.259217	Diorite	7.6	38	2.4	2207	83	467.7	15.3	83	12.5	1.0	1.8	0.2
S4	316	29.005183	33.291817	Gneiss	7.6	31	1.9	444	71	467.1	23.8	56	12.4	1.1	2.0	0.2
Group B																
B1	195	28.980600	33.295317	Diorite	14.1	30	2.3	921	84	302.9	12.7	104	12.3	1.5	1.4	0.2
B2	202	28.980600	33.295317	Gnei.Syenite	39.3	85	5.8	4923	98	289.3	5.0	185	12.5	1.0	1.5	0.2
B7	229	28.986467	33.314750	Syenite	12.5	6	1.5	38	61	221.0	27.9	69	12.7	1.6	1.7	0.2
B9	195	28.971217	33.292283	Diorite	17.4	50	2.5	1267	86	250.3	8.3	162	12.5	1.0	1.6	0.2
S6	188	29.002317	33.289000	Rhyolitic Dyke	31.3	27	4.5	1503	71	272.0	8.5	27	12.2	1.0	1.4	0.2
Z2	152	28.958000	33.287200	Gneiss	22.1	8	4.2	420	74	279.0	19.7	17	12.2	1.5	1.4	0.3
Group C																
D4	298	28.967317	33.279850	Syenite	7.6	25	0.3	61	81	83.7	10.9	11	12.7	1.2	1.4	0.2
F1	188	28.981783	33.258767	Gneiss	21.8	26	1.4	339	81	94.9	6.3	10	12.7	1.0	1.5	0.1
F3	73	28.983600	33.256667	Syenitic Dyke	41.3	17	3.5	626	89	110.2	6.5	66	12.7	1.7	1.7	0.2
F4	182	28.983600	33.256667	Gneiss	29.8	49	1.7	806	87	108.7	4.2	106	11.5	2.0	1.6	0.2
F5	189	28.993167	33.248683	Syenite	4.3	83	0.2	254	86	107.9	6.7	44	13.3	3.0	1.3	0.2

Group A (younger AFT cooling ages), B (older ZFT ages), S.-No.; samples number, [m a.s.l.]; elevation in meters above sea-level, U; Uranium concentration in µg/g, n; the number of counted apatite grains, ρ_s; density of spontaneous tracks (10⁵ tr/cm²), N_s; the number of spontaneous tracks, X²: the Chi-square test, Lc no.: number of the measured C-axis projected confined tracks, Lc: the C-axis projected confined tracks, Cen. Age: central ages with an uncertainty of 1-sigma, calculated using IsoplotR (Vermeesch, 2018).

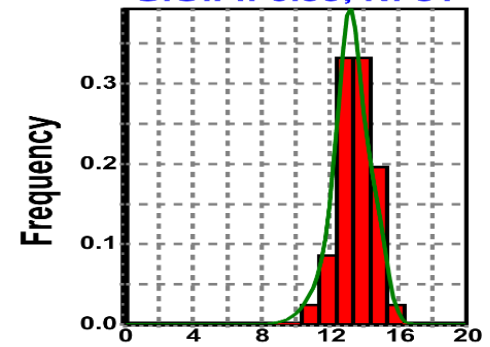
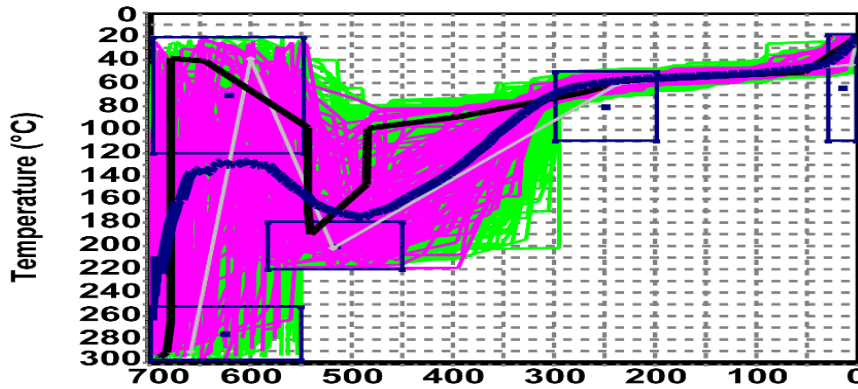
For Mansour et al. (2024a), The weighted mean ages and standard errors obtained from the ZFT thermochronometry ranged from 536 ± 14 Ma to 318 ± 9 Ma (Fig. 2), dividing into two distinct ZFT age groups (Table 1). The older group (Group A) yielded ZFT cooling ages ranging from 536 ± 14 Ma to 523 ± 15 Ma (Table 1), covering a period of approximately 13 Ma and overlapping within the uncertainty of

the measurements, with an average ZFT cooling age of 530 ± 15 Ma. The younger age group included all other samples (Fig. 2), with ZFT cooling ages between 379 ± 10 Ma and 318 ± 9 Ma, spanning a period of about 61 Ma, and overlapping within analytical errors, resulting in an average ZFT age of 331 ± 15 Ma (Table 1).

Mansour et al. (2024a)

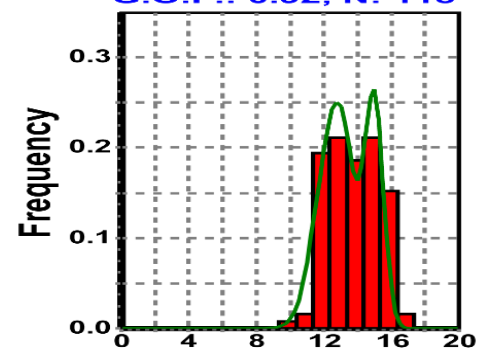
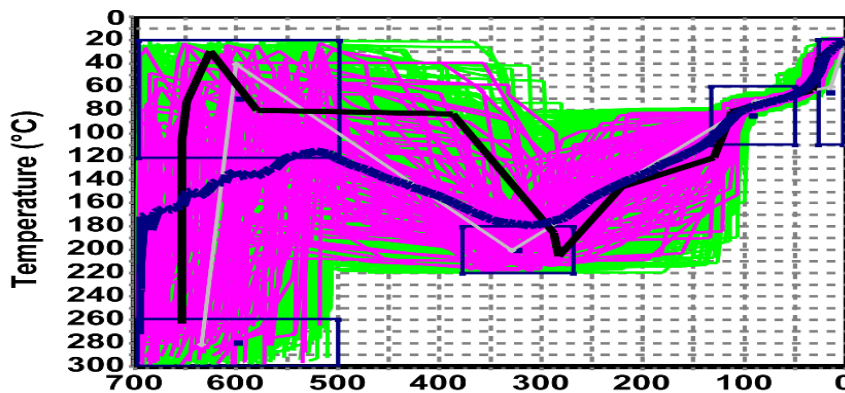
SN-12; P: 43,530 A: 517 G: 100
AFT; D: 263; M: 263±11 Ma, G.O.F.: 0.96

D: 13.28±1.17
M: 13.21±1.05
G.O.F.: 0.99, N: 81



SN-01; P: 66,703 A: 709 G: 100
AFT; D: 86.8; M: 86.6±4.9 Ma, G.O.F.: 0.98

D: 13.45±1.44
M: 13.39±1.46
G.O.F.: 0.92, N: 118



SN-03; P: 355,410 A: 1899 G: 100
AFT; D: 237; M: 237±11 Ma, G.O.F.: 0.99

D: 13.24±1.42
M: 13.18±1.50
G.O.F.: 0.87, N: 70

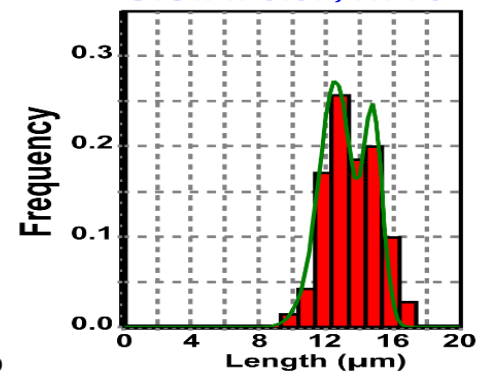
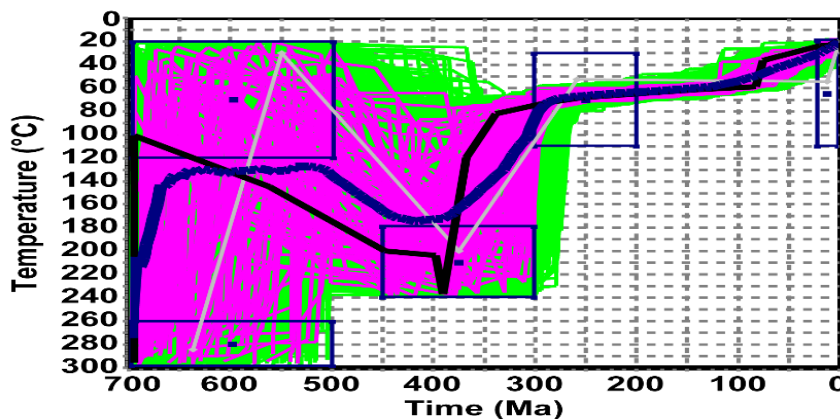
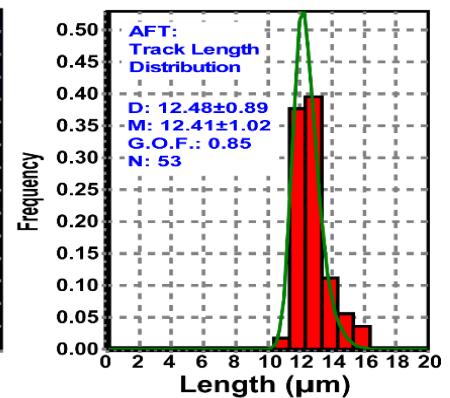
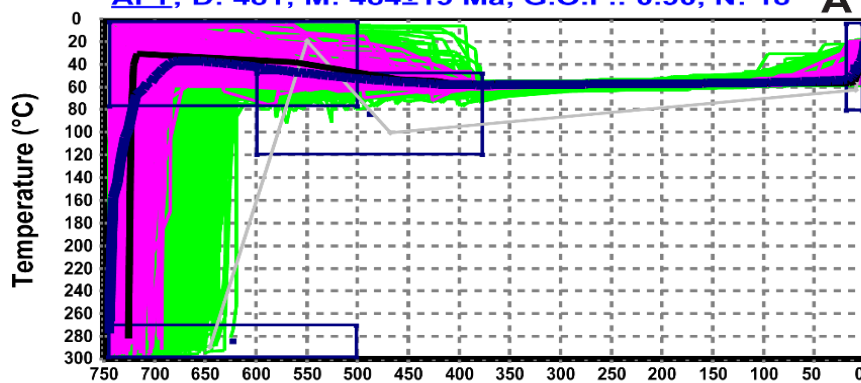


Figure 4. Thermal history models for Mansour et al. (2024a) samples were obtained using HeFTy (Ketcham et al., 2009). Resulting t–T curves show four different reliability levels: green paths: acceptable fit, purple paths: good fit, black line: best fit, and blue line: the weighted mean path (Ketcham et al., 1999, 2009). P: number of inverse iterations, A: acceptable fit models' number, G: good fit models' number, D: calculated AFT ages and CLs 1-σ error, M: model calculated AFT ages and CLs, G.O.F.: goodness of fit, N: number of single grains and CLs.

Mansour et al. (2025)

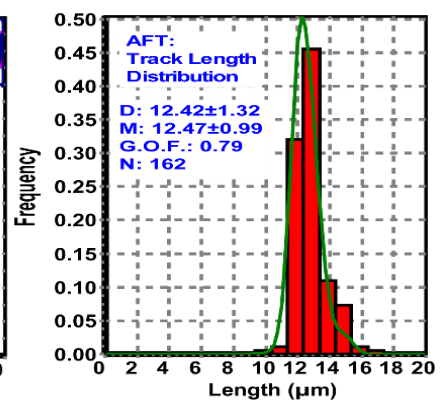
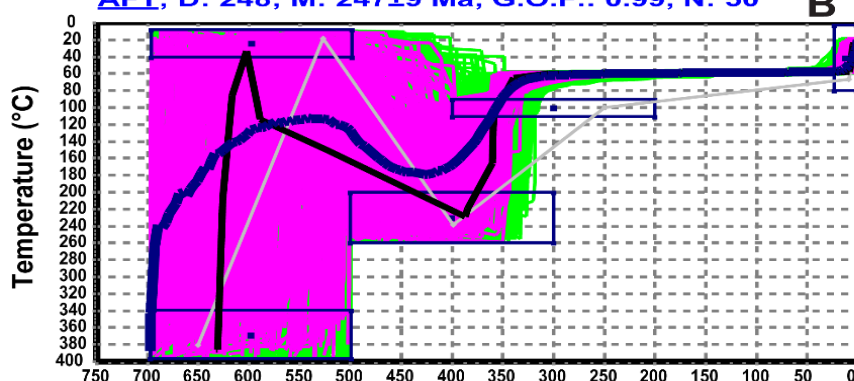
DZ; P: 200,000 A: 1506 G: 172

AFT; D: 481; M: 484±19 Ma, G.O.F.: 0.90, N: 18



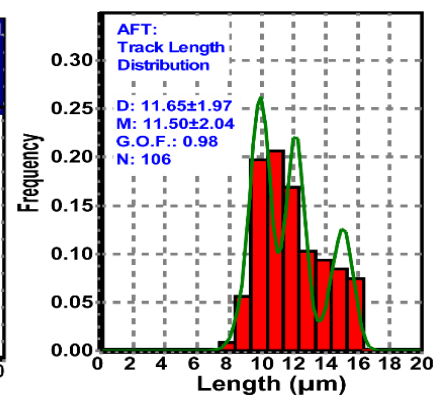
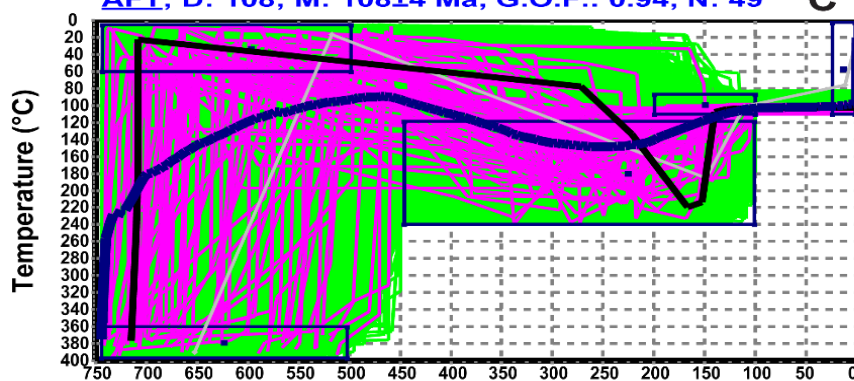
B9; P: 200,000 A: 2639 G: 318

AFT; D: 248; M: 247±9 Ma, G.O.F.: 0.99, N: 50



F4; P: 200,000 A: 2340 G: 188

AFT; D: 108; M: 108±4 Ma, G.O.F.: 0.94, N: 49



Time (Ma)

Figure 5. The samples of thermal history models for Mansour et al. (2025) were obtained using HeFTy (Ketcham et al., 2009). For more details, see Figure 4.

For the AFT analysis, the cooling ages ranged from 319 ± 15 Ma to 74 ± 5 Ma, dividing into two distinct spatiotemporal groups (Table 2). Group A consisted of three samples located along the fault zones of the Suez Rift, with Late Cretaceous cooling ages ranging from 79 ± 10 Ma to 74 ± 5 Ma (Table 2; Fig. 2), providing an average AFT cooling age of approximately 76 ± 7 Ma. Group B included the remaining 12 samples, which showed Carboniferous–Triassic cooling ages between 319 ± 15 Ma and 239 ± 11 Ma (Table 2; Fig. 2), giving an average AFT cooling age of 263 ± 13 Ma.

The t-T models indicated a generally consistent cooling scenario across the region (Figs. 4-5), except for samples from the younger AFT group, which suggested an additional cooling event (Figs. 4-5; Table 2). All modeled samples rapidly cooled during the Neoproterozoic, likely exhuming them toward the Earth's surface. This was followed by a possible reheating (burial) event that continued through the Devonian–Carboniferous period (Figs. 4-5) or even as late as the Cretaceous (Figs. 4-5). Subsequently, a second, faster cooling event occurred, leading to exhumation to the AFT Partial Annealing Zone (PAZ). Afterward, the region experienced slower cooling until the samples reached their present-day surface temperatures during the Oligocene–Miocene (Figs. 4-5).

The younger AFT group samples showed evidence of a prolonged cooling event that could extend from the Devonian–Carboniferous period through to the Cretaceous (Figs. 4-5). The intense PAEE led to the complete erosion of exposed ANS basement rocks by the Cambrian period. However, the precise position of these rocks during the Cambrian is uncertain, as they may have been either uplifted to the Earth's surface or buried. The t-T models did not conclusively support either scenario (Figs. 4-5). Nonetheless, most samples' best fit and weighted mean models suggest that the rocks were likely exhumed during the PAEE to temperatures slightly higher than the PAZ of the AFT thermochronometer.

V. Discussion and Interpretation

The older ZFT ages of Group A samples, with an average of approximately 654 ± 65 Ma for W. Ba'ba, and 530 ± 15 Ma for W. Nesyryn (Table 1, Fig. 2), point to rapid cooling shortly after the Neoproterozoic emplacement, suggesting that the region crossed the ZFT isotherm at these times. However, age-decreasing ZFT cooling ages from W. Ba'ba to W. Nesyryn suggests more southward exhumation during this event. These old ages support previous findings regarding the rapid erosion of the ANS prior to the Cambrian (Bosworth et al., 2005; Said, 1990; Seilacher, 1990). Additionally, the unconformable overlying Qebliat Group sediments, with a fluvial to nearshore marine character (Fig. 6), suggest that the area was eroded to near sea level by the Cambrian, with a marked reduction in erosional rates following the post-accretion erosional event in region A. Similar ancient ZFT ages have been recorded in other parts of the ANS (Bojar et al., 2002; Kohn et al., 2019; Kohn et al., 1992; Mansour et al., 2023b; Vermeesch et al., 2009). The second group of ages ranged from 462 ± 32 Ma to 381 ± 26 Ma for W. Ba'ba, and 379 ± 10 Ma and 318 ± 9 Ma for W. Nesyryn, aligning with previous ZFT and ZHe results from various ANS regions (Bojar et al., 2002; Kohn et al., 2019; Kohn et al., 1992; Mansour et al., 2023a; Vermeesch et al., 2009). These ages reflect a tectonic-driven uplift during the Devonian–Carboniferous period (Bojar et al., 2002; Kohn et al., 2019; Kohn et al., 1992; Mansour et al., 2023a; Vermeesch et al., 2009). The exhumation is also consistent with a sedimentary hiatus in the region between the Cambrian and Carboniferous (Fig. 6), as well as evidence for approximately 2.5 km of Lower Paleozoic clastic sediments (Kohn et al., 1992).

The AFT age groups were geographically separated into different regions, indicating a distinct tectono-thermal history for each (Table 2). This geographic variation corresponds to previously documented patterns of non-uniform block uplifting across bounding faults in the ANS (Kohn & Eyal, 1981; Mansour et al., 2023a,b,c; Omar et al., 1987, 1989; Vermeesch et al., 2009). Notably, the older thermochronological age group A was comparable to, though slightly older than, previously measured FT ages on the western rift flank (Kohn et al., 1997; Kohn & Eyal, 1981; Mansour et al., 2021; Omar et al., 1989). As with the ZFT samples, these older thermochronological ages are likely due to the rapid exhumation and erosion of the ANS following the East African Orogeny, coupled with the overlying Lower Paleozoic fluvial to nearshore marine succession (Fig. 6). The thickness of these sediments may have facilitated burial to the shallower AFT partial annealing zone depths. AFT ages of one group ranging between Permian–Triassic corresponded to the sedimentary succession, which shows multiple unconformities between formations of similar ages and Permian-age basaltic volcanics (Fig. 6). On the other hand, the other age group fall between the Lower and Upper Cretaceous, correlate with unconformities and a change in the depositional regime between the Malha and Raha formations (Fig. 6), suggesting synchronous rock uplift.

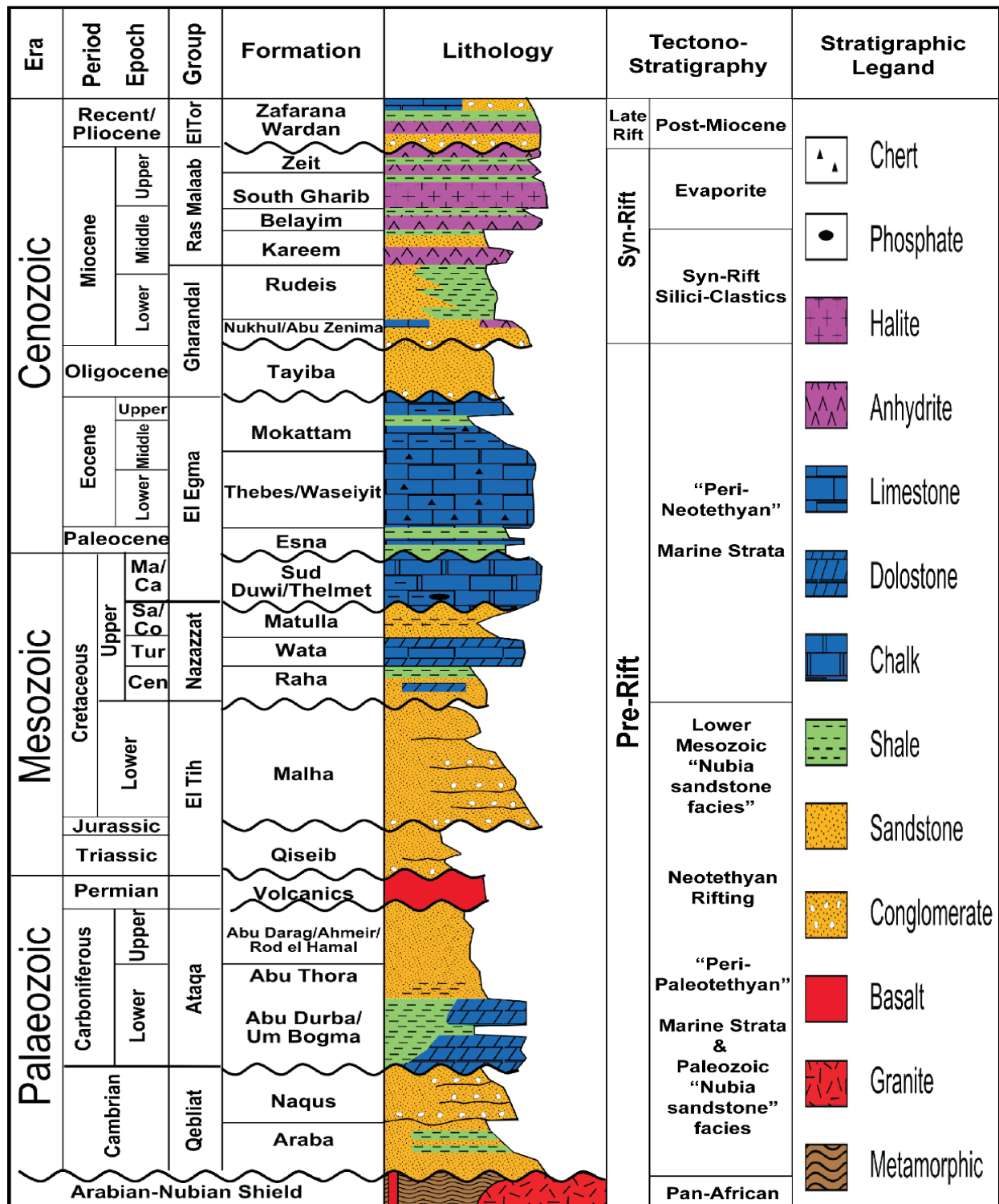


Figure 3. General lithostratigraphy of the Gulf of Suez region (Mansour et al., 2024a).

The t-T models revealed distinct cooling events for both regions, interpreted as responses to regional tectonic activities that align with known tectonic events and stratigraphic succession. The effects of these tectonic events on the studied region were evident in four main ways:

Neoproterozoic-Cambrian Cooling/Uplifting: The exhumation of rocks in response to a confirmed post-accretion erosional event, which removed the East African Orogeny shield by Cambrian time, was supported by ZFT ages (Table 1) and the Cambrian deposition of fluvial to nearshore marine sequences (Bosworth et al., 2005; Mansour et al., 2021).

Devonian-Carboniferous Cooling/Uplifting: This event, caused by the Variscan tectonic activities (Bojar et al., 2002; Mansour et al., 2024b), was reflected in AFT ages (Table 2). The sedimentary environment shifted from marine deposits in the Um Bogma Formation to terrestrial deposits in the Abu Darag Formation during the Lower and Upper Carboniferous (Fig. 6), resulting in the erosion of approximately 2–2.5 km of Lower Paleozoic sediments (Klitzsch, 1990; Mansour et al., 2023c; Moustafa & Yousif, 1993).

Late Jurassic–Early Cretaceous Cooling/Uplifting: The Gondwana disintegration during this period caused localized doming on the northern African margin, northern and central Sinai, and the Gulf of Suez region (Awad, 1984; Bojar et al., 2002; Feinstein et al., 2013; Mansour et al., 2023b; Said, 1962; Sakran et al., 2019; Sestini, 1984). AFT ages (Table 2) and several unconformities (Fig. 6) indicate the exhumation during this time. The region's localized uplifting events were likely influenced by fault activation in line with the stress field associated with each event, with similar reports from Sinai's northern and central regions (Moustafa et al., 2003).

Oligocene-Miocene Cooling/Uplifting: This cooling event, attributed to the rifting of the Gulf of Suez, was reflected in the deposition of syn-rift sediments (Fig. 6) and the absence of high topography prior to rifting (Bosworth et al., 2015; Bosworth & Stockli, 2016; Garfunkel, 1988). AFT modeling indicated that exhumation occurred at temperatures below 110°C, consistent with track length distributions suggesting exhumation from the AFT partial annealing zone (110–60°C), with the modeling indicating temperatures between 80 and 60°C (Figs. 4-5).

VI. Conclusions

The northern termination of the ANS has experienced a complex tectonic history over geological time. Initially formed during the Neoproterozoic as part of the East African Orogeny, the region underwent significant erosion by the end of the Cambrian period. This erosion likely resulted in an isostatic rebound, causing a substantial uplift of the rocks. In the aftermath, approximately 2 to 2.5 km of Lower Paleozoic sedimentary strata were deposited atop the ANS basement rocks. The subsequent Variscan tectonic event during the Devonian-Carboniferous period triggered differential rock uplifts in the region, removing the entire Lower Paleozoic sedimentary succession. After this tectonic activity, the region entered a period of tectonic-thermal stability, characterized by non-tectonic erosion, which continued until the Cretaceous period. The disintegration of Gondwana during the Cretaceous had a differential impact on the region where a cooling/exhumation event occurred. In the Miocene, the region experienced a significant uplift of approximately 1.4 ± 0.2 km as the northeastern flank of the Gulf of Suez rift began to form. After this, the region's topography underwent reshaping through non-tectonic processes, eventually reaching its current elevation.

The tectonic history of the northwestern region of the Sinai basement shows the effects of both imminent and far-field stresses. Imminent events, such as the post-accretion erosional event and the Suez rifting, resulted in widespread exhumation across the region. In contrast, far-field stresses, including the Variscan orogeny and the opening of the mid-Atlantic, led to differential rock uplifts at specific locations, shaping the present-day geological landscape.

References

1. Alsharhan, A. S., & Nairn, A. E. M. (1997). *Sedimentary Basins and Petroleum Geology of the Middle East*. Elsevier. <https://doi.org/10.1016/B978-0-444-82465-3.X5000-1>
2. Awad, G. M. (1984). *Habitat of oil in Abu Gharadiq and Faiyum basins, Western Desert, Egypt*. 68, 564–573.
3. Bojar, A.-V., Fritz, H., Kargl, S., & Unzog, W. (2002). Phanerozoic tectonothermal history of the Arabian–Nubian shield in the Eastern Desert of Egypt: Evidence from fission track and paleostress data. *Journal of African Earth Sciences*, 34(3–4), 191–202. [https://doi.org/10.1016/S0899-5362\(02\)00018-0](https://doi.org/10.1016/S0899-5362(02)00018-0)
4. Bosworth, W., Huchon, P., & McClay, K. (2005). The Red Sea and Gulf of Aden Basins. *Journal of African Earth Sciences*, 43(1–3), 334–378. <https://doi.org/10.1016/j.jafrearsci.2005.07.020>
5. Bosworth, W., & Stockli, D. F. (2016). Early magmatism in the greater Red Sea rift: Timing and significance. *Canadian Journal of Earth Sciences*, 53(11), 1158–1176. <https://doi.org/10.1139/cjes-2016-0019>
6. Bosworth, W., Stockli, D. F., & Helgeson, D. E. (2015). Integrated outcrop, 3D seismic, and geochronologic interpretation of Red Sea dike-related deformation in the Western Desert, Egypt – The role of the 23Ma Cairo “mini-plume.” *Journal of African Earth Sciences*, 109, 107–119. <https://doi.org/10.1016/j.jafrearsci.2015.05.005>
7. Dewey, J. F., Pitman, W. C., Ryan, W. B. F., & Bonnin, J. (1973). Plate Tectonics and the Evolution of the Alpine System. *Geological Society of America Bulletin*, 84(10), 3137. [https://doi.org/10.1130/0016-7606\(1973\)84<3137:PTATEO>2.0.CO;2](https://doi.org/10.1130/0016-7606(1973)84<3137:PTATEO>2.0.CO;2)
8. Feinstein, S., Eyal, M., Kohn, B. P., Steckler, M. S., Ibrahim, K. M., Moh’d, B. K., & Tian, Y. (2013). Uplift and denudation history of the eastern Dead Sea rift flank, SW Jordan: Evidence from apatite fission track thermochronometry: UPLIFT HISTORY OF DEAD SEA RIFT FLANK. *Tectonics*, 32(5), 1513–1528. <https://doi.org/10.1002/tect.20082>
9. Garfunkel, Z. (1988). *Relation between continental rifting and uplifting – evidence from the Suez Rift and northern Red-Sea*. 150(1–2), 33–49.
10. Garfunkel, Z., & Derin, B. (1985). Permian-Early Mesozoic tectonism and continental margin formation in Israel and its implications for the history of the Eastern Mediterranean. In J. E. Dixon & A. H. F. Robertson (Eds.), *The geological evolution of the eastern Mediterranean* (Special Publication of the Geological Society, Vol. 17, pp. 187–201). Blackwell.
11. Girdler, R. W. (1985). Problems concerning the evolution of oceanic lithosphere in the northern Red Sea. *Tectonophysics*, 116(1), 109–122. [https://doi.org/10.1016/0040-1951\(85\)90224-0](https://doi.org/10.1016/0040-1951(85)90224-0)
12. Gleadow, A. J. W., & Duddy, I. R. (1981). A natural long-term track annealing experiment for apatite. *Nuclear Tracks*, 5(1–2), 169–174. [https://doi.org/10.1016/0191-278X\(81\)90039-1](https://doi.org/10.1016/0191-278X(81)90039-1)
13. Greiling, R. O., Kriiner, A., El Ramly, M. F., & Rashwan, A. A. (1988). Structural relationships between the southern and central parts of the Eastern Desert of Egypt: Details of a fold and thrust belt. In S. El Gaby & R. O. Greiling (Eds.), *The Pan-African of NE Africa and Adjacent Areas* (pp. 121–145). Vieweg.
14. Gvirtzman, G., & Weissbrod, T. (1984). The Hercynian Geanticline of Helez and the Late Palaeozoic history of the Levant. *Geological Society, London, Special Publications*, 17(1), 177–186. <https://doi.org/10.1144/GSL.SP.1984.017.01.11>
15. Hashad, M. H. (1980). *Contribution to the mineralogy and geochemistry of some carbonate rocks in the basement complex of Egypt* [Ph.D. Thesis]. AI Azhar University.
16. Kennedy, W. Q. (1964). *The Structural Differentiation of Africa in the Pan-African (±500 m.y.) Tectonic Episode*. 8, 48–49.
17. Klitzsch, E. (1986). Plate tectonics and cratonal geology in Northeast Africa (Egypt, Sudan). *Geologische Rundschau*, 75(3), 755–768. <https://doi.org/10.1007/BF01820645>
18. Klitzsch, E. (1990). Paleozoic. In R. Said (Ed.), *The Geology of Egypt* (2nd ed., Vol. 24, pp. 451–486). Balkema, Rotterdam.

19. Kohn, B. P., & Eyal, M. (1981). History of uplift of the crystalline basement of Sinai and its relation to opening of the Red Sea as revealed by fission track dating of apatites. *Earth and Planetary Science Letters*, 52(1), 129–141. [https://doi.org/10.1016/0012-821X\(81\)90215-6](https://doi.org/10.1016/0012-821X(81)90215-6)
20. Kohn, B. P., Eyal, M., & Feinstein, S. (1992). A major Late Devonian-Early Carboniferous (Hercynian) Thermotectonic event at the NW Margin of the Arabian-Nubian Shield: Evidence from zircon fission track dating. *Tectonics*, 11(5), 1018–1027. <https://doi.org/10.1029/92TC00636>
21. Kohn, B. P., Feinstein, S., Foster, D. A., Steckler, M. S., & Eyal, M. (1997). Thermal history of the eastern Gulf of Suez, II. Reconstruction from apatite fission track and K-feldspar measurements. *Tectonophysics*, 283(1–4), 219–239. [https://doi.org/10.1016/S0040-1951\(97\)00069-3](https://doi.org/10.1016/S0040-1951(97)00069-3)
22. Kohn, B., Weissbrod, T., Chung, L., Farley, K., & Bodorkos, S. (2019). Low-temperature thermochronology of francolite: Insights into timing of Dead Sea Transform motion. *Terra Nova*, 31(3), 205–219. <https://doi.org/10.1111/ter.12387>
23. Kolodner, K., Avigad, D., McWILLIAMS, M., Wooden, J. L., Weissbrod, T., & Feinstein, S. (2006). Provenance of north Gondwana Cambrian–Ordovician sandstone: U–Pb SHRIMP dating of detrital zircons from Israel and Jordan. *Geological Magazine*, 143(3), 367–391. <https://doi.org/10.1017/S0016756805001640>
24. Kröner, A., Eyal, M., & Eyal, Y. (1990). Early Pan-African evolution of the basement around Elat, Israel, and the Sinai Peninsula revealed by single-zircon evaporation dating, and implications for crustal accretion rates. *Geology*, 18(6), 545. [https://doi.org/10.1130/0091-7613\(1990\)018<0545:EPAEOT>2.3.CO;2](https://doi.org/10.1130/0091-7613(1990)018<0545:EPAEOT>2.3.CO;2)
25. Kröner, A., Kröger, J., & Rashwan, A. A. A. (1994). Age and tectonic setting of granitoid gneisses in the Eastern Desert of Egypt and south-west Sinai. *Geologische Rundschau*, 83(3), Article 3. <https://doi.org/10.1007/BF00194157>
26. Mansour, S. (2015). *Long-term topographic evolution of the African plate, causes and consequences for surrounding lithospheric plates* [Universität Heidelberg]. <https://doi.org/10.11588/heidok.00020122>
27. Mansour, S. (2023a). Tectonic Development of Wadi Mi'ar Area, Sinai, Egypt: Implications of Low-Temperature Thermochronology Techniques. *Alfarama Journal of Basic & Applied Sciences*, 4(4), 727–738. <https://doi.org/10.21608/ajbas.2023.218033.1160>
28. Mansour, S., Abdelfadil, K. M., Hasebe, N., Tamura, A., Abdelrahman, K., Gharib, M. A., Fnais, M. S., & Shehata, A. A. (2024a). Thermochronological Constraints on the Tectonic History of the Arabian–Nubian Shield's Northern Tip, Sinai, Egypt. *Minerals*, 14(12), 1246. <https://doi.org/10.3390/min14121246>
29. Mansour, S., Gharib, M. A., Hasebe, N., Abdelrahman, K., Fnais, M. S., & Tamura, A. (2023b). Tectonic evolution of the Gabal Loman area, North Eastern Desert, Egypt: Implications from low-temperature multithermochronometry on the Arabian-Nubian shield. *Frontiers in Earth Science*, 11(1193692), 15. <https://doi.org/doi:10.3389/feart.2023.1193692>
30. Mansour, S., Glasmacher, U. A., Krob, F. C., Casillas, R., & Albinger, M. (2022b). Timing of rapid cooling and erosional decay of two volcanic islands of the Canary Archipelago: Implications from low-temperature thermochronology. *International Journal of Earth Sciences*. <https://doi.org/10.1007/s00531-022-02253-7>
31. Mansour, S., Hasebe, N., Abdelrahman, K., Fnais, M. S., Gharib, M. A., Habou, R., & Tamura, A. (2024b). Development of the Arabian-Nubian Shield along the Marsa Alam-Idfu transect, Central-Eastern Desert, Egypt: Geochemical implementation of zircon U-Pb geochronology. *Geochemical Transactions*, 25(1). <https://doi.org/10.1186/s12932-024-00095-7>
32. Mansour, S., Hasebe, N., Abdelrahman, K., Fnais, M. S., & Tamura, A. (2023c). Reconstructing the Tectonic History of the Arabian–Nubian Shield in Sinai: Low-Temperature Thermochronology Implications on Wadi Agar Area. *Minerals*, 13(4), Article 4. <https://doi.org/10.3390/min13040574>
33. Mansour, S., Hasebe, N., Abdelrahman, K., Fnais, M. S., & Tamura, A. (2024c). The Gulf of Suez rifting: Implications from low-temperature thermochronology. *International Geology Review*, 1–17. <https://doi.org/10.1080/00206814.2024.2400695>
34. Mansour, S., Hasebe, N., Azab, E., Elnaggar, A. Y., & Tamura, A. (2021). Combined Zircon/Apatite U-Pb and Fission-Track Dating by LA-ICP-MS and Its Geological Applications: An Example from the Egyptian Younger Granites. *Minerals*, 11(12), Article 12. <https://doi.org/10.3390/min11121341>

35. Mansour, S., Hasebe, N., Glasmacher, U. A., Tamura, A., & El-Shafei, M. K. (2025). New insights into the thermo-tectonic development of the Suez rift within the framework of the northern Arabian–Nubian Shield. *Earth Surface Processes and Landforms*, 50(1). <https://doi.org/10.1002/esp.6054>
36. Mansour, S., Hasebe, N., Khedr, M. Z., Tamura, A., & Shehata, A. A. (2023d). Tectonic-Thermal Evolution of the Wadi El-Dahal Area, North Eastern Desert, Egypt: Constraints on the Suez Rift Development. *Minerals*, 13(8), Article 8. <https://doi.org/10.3390/min13081021>
37. Mansour, S., Hasebe, N., Meert, J. G., Tamura, A., Khalaf, F. I., & El-Shafei, M. K. (2022a). Evolution of the Arabian-Nubian Shield in Gabal Samra area, Sinai; implications from zircon U–Pb geochronology. *Journal of African Earth Sciences*, 192, 104538. <https://doi.org/10.1016/j.jafrearsci.2022.104538>
38. Mansour, S., Hasebe, N., & Tamura, A. (2023e). Erosional reservoir for the northern segment of the Arabian-Nubian shield: Constrains from U-Pb geochronology of the lower palaeozoic succession, North Eastern Desert, Egypt. *Precambrian Research*, 388, 107017. <https://doi.org/10.1016/j.precamres.2023.107017>
39. Mansour, S., Hasebe, N., Tamura, A., Abdelrahman, K., Fnais, M. S., Gharib, M. A., & Khedr, M. Z. (2024d). Geochronological assessment of the Arabian-Nubian Shield plutonic intrusions in the arc assemblages along the Qift-Quseir transect, Central Eastern Desert of Egypt. *Journal of African Earth Sciences*, 220, 105456. <https://doi.org/10.1016/j.jafrearsci.2024.105456>
40. Meert, J. G. (2003). A synopsis of events related to the assembly of eastern Gondwana. *Tectonophysics*, 362(1–4), 1–40. [https://doi.org/10.1016/S0040-1951\(02\)00629-7](https://doi.org/10.1016/S0040-1951(02)00629-7)
41. Meneisy, M. Y. (1986). Mesozoic igneous activity in Egypt. *Qatar University Science Bulletin*, 6.
42. Moustafa, A. R., Saoudi, A., Moubasher, A., Ibrahim, I. M., Molokhia, H., & Schwartz, B. (2003). Structural setting and tectonic evolution of the Bahariya Depression, Western Desert, Egypt. *GeoArabia*, 8(1), 91–124. <https://doi.org/10.2113/geoarabia080191>
43. Moustafa, A. R., & Yousif, M. S. M. (1993). Structural evolution of the eastern shoulder of the Suez Rift: Um Bogma area. *Neues Jahrbuch Für Geologie Und Paläontologie - Monatshefte*, 1993(11), 655–668. <https://doi.org/10.1127/njgpm/1993/1993/655>
44. Omar, G. I., Kohn, B. P., Lutz, T. M., & Faul, H. (1987). The cooling history of Silurian to Cretaceous alkaline ring complexes, south Eastern Desert, Egypt, as revealed by fission-track analysis. *Earth and Planetary Science Letters*, 83(1–4), 94–108. [https://doi.org/10.1016/0012-821X\(87\)90054-9](https://doi.org/10.1016/0012-821X(87)90054-9)
45. Omar, G. I., & Steckler, M. S. (1995). Fission Track Evidence on the Initial Rifting of the Red Sea: Two Pulses, No Propagation. *Science*, 270(5240), 1341–1344. <https://doi.org/10.1126/science.270.5240.1341>
46. Omar, G. I., Steckler, M. S., Buck, W. R., & Kohn, B. P. (1989). Fission-track analysis of basement apatites at the western margin of the Gulf of Suez rift, Egypt: Evidence for synchronicity of uplift and subsidence. *Earth and Planetary Science Letters*, 94(3–4), 316–328. [https://doi.org/10.1016/0012-821X\(89\)90149-0](https://doi.org/10.1016/0012-821X(89)90149-0)
47. Patchett, P., & Chase, C. (2002). Role of transform continental margins in major crustal growth episodes. *Geology*, 30. [https://doi.org/10.1130/0091-7613\(2002\)030<0039:ROTCMI>2.0.CO;2](https://doi.org/10.1130/0091-7613(2002)030<0039:ROTCMI>2.0.CO;2)
48. Platt, J. P., & England, P. C. (1994). Convective removal of lithosphere beneath mountain belts; thermal and mechanical consequences. *American Journal of Science*, 294(3), 307–336. <https://doi.org/10.2475/ajs.294.3.307>
49. Said, R. (1962). *The Geology of Egypt* (1st ed.). Elsevier, Amsterdam.
50. Said, R. (1990). *The Geology of Egypt* (2nd ed.). A.A. Balkema, Rotterdam.
51. Sakran, S., Shehata, A. A., Osman, O., & El-Sherbiny, M. (2019). Superposed tectonic regimes in west Beni Suef basin, Nile Valley, Egypt: Implications to source rock maturation and hydrocarbon entrapment. *Journal of African Earth Sciences*, 154, 1–19. <https://doi.org/10.1016/j.jafrearsci.2019.03.010>
52. Schott, B., & Schmeling, H. (1998). Delamination and detachment of a lithospheric root—ScienceDirect. *Tectonophysics*, 296(3–4), 225–247.
53. Seilacher, A. (1990). Paleozoic trace fossils. In R. Said (Ed.), *The Geology of Egypt* (pp. 649–670). Balkema, Rotterdam.
54. Sestini, G. (1984). Tectonic and sedimentary history of the NE African margin (Egypt—Libya). *Geological Society, London, Special Publications*, 17(1), 161–175. <https://doi.org/10.1144/GSL.SP.1984.017.01.10>

55. Shehata, A. A., El Fawal, F. M., Ito, M., Aboulmagd, M. A., & Brooks, H. L. (2020). Senonian platform-to-slope evolution in the tectonically-influenced Syrian Arc sedimentary belt: Beni Suef Basin, Egypt— ScienceDirect. *Journal of African Earth Sciences*, 170, <https://doi.org/10.1016/j.jafrearsci.2020.103934>.
56. Stampfli, G. M., von Raumer, J. F., & Borel, G. D. (2002). Paleozoic evolution of pre-Variscan terranes: From Gondwana to the Variscan collision. In J. R. M. Catalán, R. D. Hatcher, R. Arenas, & F. D. García, *Variscan-Appalachian dynamics: The building of the late Paleozoic basement*. Geological Society of America. <https://doi.org/10.1130/0-8137-2364-7.263>
57. Steckler, M. S., Feinstein, S., Kohn, B. P., Lavier, L. L., & Eyal, M. (1998). Pattern of mantle thinning from subsidence and heat flow measurements in the Gulf of Suez: Evidence for the rotation of Sinai and along-strike flow from the Red Sea. *Tectonics*, 17(6), 903–920. <https://doi.org/10.1029/1998TC900002>
58. Stern, R. J., & Hedge, C. E. (1985). Geochronologic and isotopic constraints on late Precambrian crustal evolution in the Eastern Desert of Egypt. *American Journal of Science*, 285(2), 97. <https://doi.org/10.2475/ajs.285.2.97>
59. Stern, R. J., Johnson, P. R., Kröner, A., & Yibas, B. (2004). Neoproterozoic Ophiolites of the Arabian-Nubian Shield. In *Developments in Precambrian Geology* (Vol. 13, pp. 95–128). Elsevier. [https://doi.org/10.1016/S0166-2635\(04\)13003-X](https://doi.org/10.1016/S0166-2635(04)13003-X)
60. Stern, R. J., & Manton, W. I. (1987). Age of Feiran basement rocks, Sinai: Implications for late Precambrian crustal evolution in the northern Arabian–Nubian Shield. *Journal of the Geological Society*, 144(4), 569–575. <https://doi.org/10.1144/gsjgs.144.4.0569>
61. Vermeesch, P., Avigad, D., & McWilliams, M. O. (2009). 500 m.y. Of thermal history elucidated by multi-method detrital thermochronology of North Gondwana Cambrian sandstone (Eilat area, Israel). *GSA Bulletin*, 121(7–8), 1204–1216. <https://doi.org/10.1130/B26473.1>
62. Wagner, G. A. (1972). Spaltspurenalter von Mineralen und natürlichen Gläsern: Eine Übersicht. *Fortschritte Der Mineralogie*, 49, 114–145.
63. Yamada, R., Tagami, T., Nishimura, S., & Ito, H. (1995). Annealing kinetics of fission tracks in zircon: An experimental study. *Chemical Geology*, 122(1–4), 249–258. [https://doi.org/10.1016/0009-2541\(95\)00006-8](https://doi.org/10.1016/0009-2541(95)00006-8)



Open Access Journal

© 2025 by the authors. Disclaimer/Publisher's Note: The content in all publications reflects the views, opinions, and data of the respective individual author(s) and contributor(s), and not those of the scientific association for studies and applied research (SASAR) or the editor(s). SASAR and/or the editor(s) explicitly state that they are not liable for any harm to individuals or property arising from the ideas, methods, instructions, or products mentioned in the content.